1992ApJ...385..522G

THE ASTROPHYSICAL JOURNAL, 385:522–535, 1992 February 1

STRUCTURE, CHEMISTRY, AND CLUMPING IN THE NGC 2071 (NORTH) MOLECULAR CLOUD

PAUL F. GOLDSMITH, MICHAEL MARGULIS,[1] AND RONALD L. SNELL
Five College Radio Astronomy Observatory, Department of Physics and Astronomy, University of Massachusetts, Amherst, MA 01003
AND
Y. FUKUI
Department of Astrophysics, Nagoya University, Chikusa-ku Nagoya 464, Japan

Received 1991 May 28; accepted 1991 August 7

ABSTRACT

We have carried out a study of the NGC 2071 (North) molecular cloud in the 3 mm wavelength transitions of CO, ^{13}CO, $C^{18}O$, CS, and HCO^+ using the FCRAO 14 m telescope. We find that the distribution of CS and $C^{18}O$, two tracers that are widely used to trace dense gas in molecular clouds, are very different, and that they both differ appreciably from the previously published distribution of NH_3. The $C^{18}O$, CS, and NH_3 are all highly clumped; using the standard value for the fractional abundance of $C^{18}O$, we find that the four prominent clumps seen in this species are unbound. The explanation of the structure and chemical differentiation in this region may lie in the presence of an outflow which we find to be centered on the 26–40 $L_\odot$ source IRAS 05451+0037. The single significant peak of the CS emission coincides with the infrared source, one of the four ammonia peaks occurs there, while none of the other tracers has a significant maximum at this position. We suggest that the molecular abundances in this relatively large region have been significantly affected by the outflow and presence of the young stellar object. This effect, which may be relatively common, indicates that the apparent morphology of molecular clouds with recent star formation may be highly dependent on the molecular tracer used as a result of variations in the fractional abundances of different species.

Subject headings: ISM: individual (NGC 2071) — ISM: molecules — ISM: structure — molecular processes

1. INTRODUCTION

The effects of star formation on molecular material surrounding the newly formed luminous sources have been the subject of considerable investigation in recent years. Massive stars produce great compositional changes as a result of the ionization they produce, and the considerable overpressure of the H II region in turn has a major dynamical impact on neighboring molecular material (cf. Tenorio-Tagle 1982). Lower mass stars, while less dramatic in their effects, have been found to go through a phase in which they inject considerable mechanical energy is to surrounding material by means of an atomic and/or molecular wind, producing an outflow of swept-up molecular gas (cf. Snell 1989).

Of considerable interest is the effect on the chemistry of surrounding, relatively quiescent material produced by the young stellar objects. While complicated to unravel in the presence of excitation gradients and radiative transfer effects, chemical abundance variations have been observed in a number of objects with both high- and low-mass star formation taking place. Some examples include Sgr B2 (Goldsmith et al. 1987; Vogal, Genzel, & Palmer 1987; Lis & Goldsmith 1991), Orion A (Plambeck & Wright 1988), NGC 2071 (Zhou, Evans, & Mundy 1990), and L134N (Swade 1989a, b). A significant change in the composition of the molecular gas can alter other physical conditions in these regions; for example, if the abundance of an important coolant changes appreciably, the temperature of the region will also be affected. From the point of view of understanding the star formation process and its effects on molecular clouds, alteration of the chemical composition is also potentially very important, since our understanding of the complex regions depends to a large degree on the assumption that certain *tracers* probe gas with particular characteristic values of density, temperature, etc. (Goldsmith 1991).

Modification of the composition of the gas surrounding young stars can take place through a number of mechanisms. A relatively mild effect is warming of dust grains with subsequent liberation of molecules frozen onto grain surfaces (as proposed for the hot core in Orion by Plambeck & Wright 1988). Temperature and density changes are likely to occur in the surrounding material as a result of the effects of stellar winds; these can have an effect on chemical reaction rates, and also on the shielding of molecules from both internal and external sources of radiation. It has also been recognized for some time that energy imparted to molecules by shocks would be sufficient to overcome energy barriers which prevent certain endothermic reactions from taking place at a significant rate in general molecular cloud material (e.g., Mitchell & Deveau 1982, 1983; Draine, Roberge, & Dalgarno 1983; Mitchell 1984; Dalgarno 1985). The potential importance of these effects suggests that the models of clouds should incorporate the effects of young stars into the chemical evolution of these regions. A suggestion of non–steady state chemistry in a dark cloud with multiple outflows and a high degree of clumpiness of the quiescent gas was made by Goldsmith, Langer, & Wilson (1986). More recently, a number of theoretical investigations of chemical evolution in the environment of winds driven by a low-mass young stellar object have been carried out (Charnley & Williams 1990; Charnley et al. 1990; Nejad, Williams, & Charnley 1990). These studies are necessarily limited by the

---

[1] Postal address: General Electric Astrospace Division, 230 E. Goddard Boulevard, King of Prussia, PA 19406.

complexity of the regions with which they are concerned and by the lack of data presently available to constrain the models.

The present project was carried out to address the issue of the chemistry of regions with outflows, with primary emphasis on analysis of commonly used tracers of dense gas. We have chosen NGC 2071 (North) [NGC 2071(N)] as an example of a relatively nearby ($D \cong 400$ pc; Anthony-Twarog 1982) region with an embedded infrared source of modest luminosity (40 $L_{\odot}$) which contains a somewhat ill-defined molecular outflow (Fukui et al. 1986; Iwata, Fukui, & Ogawa 1988, hereafter IFO). IFO also found that the distributions of the $C^{18}O$ and NH_3 emission were significantly different within this region, suggesting that there might be some chemical differentiation between these two tracers of dense gas. We have carried out observations of the 3 mm wavelength transitions of CO, ^{13}CO, $C^{18}O$, CS, and HCO^+ using the FCRAO 14 m telescope, and used these together with the published NH_3 data to obtain information about the morphology of the outflow, the degree of clumping in the emission from various species, and the relationship of the highly nonuniform emission at the quiescent cloud velocity seen in most species to the high-velocity outflow. The observations and basic data reduction techniques are discussed in § 2, and a detailed discussion is presented in §§ 3 and 4.

2. OBSERVATIONS

The millimeter-wavelength observations were carried out with the radome-enclosed FCRAO 14 m telescope during several observing sessions between 1989 October and 1990 April. The receiver was a cooled Schottky diode mixer with quasi-optical single-sideband filter and cooled image termination. The system temperature varied significantly between the different lines observed, primarily as a result of the differing atmospheric opacity. Single-sideband system temperatures referred to above the Earth's atmosphere were typically 350 K for CS and HCO^+ observations, 500 K for ^{13}CO and $C^{18}O$ observations, and 700 K for ^{12}CO observations. The pointing and focus of the antenna were checked by observations of Jupiter, which was relatively close to NGC 2071(N).

The data were obtained in a position-switched mode, with a reference position offset relative to the map center position by 60′ in right ascension; each reference observation was used with data for three on-source positions. Integration time was built up by repeating maps as required, with final statistical uncertainties given in Table 1. The entries in this table as well as in the figures refer to T_R^*, the antenna temperature corrected for the forward spillover and scattering efficiency $\eta_{\rm fss}$ ($T_R^* = T_A^*/\eta_{\rm fss}$; Kutner & Ulich 1981), where T_A^* is the antenna temperature obtained using the usual chopper-wheel calibration method. For the 14 m telescope, $\eta_{\rm fss}$ varies somewhat with frequency; we have here adopted a value of 0.75, for all the transitions observed, which is not in error by more than 5%.

TABLE 1

STATISTICAL UNCERTAINTIES FOR OBSERVED MOLECULAR SPECIES

	SPECIES				
UNCERTAINTY	^{12}CO	^{13}CO	$C^{18}O$	CS	HCO^+
T_R^{*}[a]	0.4	0.4	0.14	0.11	0.11
$\int T_R^* dv$[b]	0.5 (0.4)[c]	0.59[d]	0.15[e]	0.12[e]	0.13[f]

[a] Root mean square uncertainty in a single 100 kHz channel in K.

[b] Root mean square uncertainty in velocity interval specified for each species in K km s^{-1}.

[c] $\Delta v = 4$ km s^{-1} (11–15 km s^{-1}) for redshifted emission and $\Delta v = 6$ km s^{-1} (0–6 km s^{-1}) for blueshifted emission.

[d] $\Delta v = 8$ km s^{-1} (5–13 km s^{-1}).

[e] $\Delta v = 4$ km s^{-1} (7–11 km s^{-1}).

[f] $\Delta v = 4.5$ km s^{-1} (6.75–11.25 km s^{-1}).

The data are presented in the form of contour maps in Figures 1–3, with offsets in arcminutes relative to $\alpha_{1950} = 05^{\rm h}45^{\rm m}00^{\rm s}$, $\delta_{1950} = 00°39'00''$. Figure 1 includes the ^{12}CO $J = 1$–0 peak T_R^* data from the 14 m antenna, and the NH_3 $(J, K) = (1, 1)$ data of IFO, which give the peak intensity of this line. The angular resolution of the NH_3 data obtained with the Effelsberg antenna is comparable to that of the millimeter-wavelength lines observed at FCRAO. For the NH_3 data the lowest contour plotted is at the 0.9 K level, and the contour spacing is 0.45 K. The ^{12}CO maximum intensity shows very little variation over the region mapped. The lowest contour for this species in Figure 1 is at 8.8 K, the highest contour is at 11.2 K, and the contour spacing is 0.8 K, twice the rms uncertainty in T_R^*. These choices obviously highlight the variations in intensity that are present.

Based on the expectation (discussed further below) that the integrated intensity of the lines of the other species we have observed may trace the total column density, the panels of Figure 2 show the distribution of integrated intensity of the $J = 1$–0 transitions of ^{13}CO, $C^{18}O$, and HCO^+, and the $J = 2$–1 transition of CS. The ^{13}CO emission is quite strong and relatively uniform (compared with the other lines shown in Fig. 2). The lowest contour level, 7.0 K km s^{-1}, is approximately 12 times the rms uncertainty in the integrated intensity. For the weaker $C^{18}O$, CS, and HCO^+ lines, the lowest contour plotted and the contour spacing are both equal to three times the rms uncertainty in the integrated intensity. The integration range for the ^{13}CO emission is chosen to be 8 km s^{-1} rather than the 4 km s^{-1} used for the other tracers, due to the greater line width of this species.

The integrated intensity of ^{12}CO in the red- and blueshifted wings is shown in Figure 3, which also includes the position of the infrared source IRAS 04541+0037 and three Hα emission T Tauri stars studied by Herbig & Kuhi (1963). The differing line intensities and velocity widths of the red- and blueshifted gas make the signal-to-noise ratio vary different in the two line wings. The redshifted emission is integrated over the 11–15 km s^{-1} velocity interval, having an rms uncertainty of 0.5 K km s^{-1} and lowest contour and contour spacing at 2 and 1 K km s^{-1}, respectively. The blueshifted emission is integrated over the 0–6 km s^{-1} range and has an rms uncertainty of 0.4 K km s^{-1}, lowest contour 2.5 K km s^{-1}, and contour spacing 1.5 K km s^{-1}. We present the results of the observations individually in the sections which follow, and make intercomparisons in § 4.

3. RESULTS

3.1. ^{12}CO *Emission at Ambient Cloud Velocity*

This emission is relatively uniform and extended. If we thus take the coupling efficiency to a 30′ source to be unity, the range of radiation temperatures T_R^* of 8–10.4 K corresponds to kinetic temperatures between 11 and 14 K. These temperatures are only slightly warmer than expected for quiescent, well-shielded molecular cloud material. The luminosity of the infrared source IRAS 05451+0037 is, according to IFO, 40 $L_{\odot}$.[2] Its output should warm the dust in a 1′ radius region to approximately 25 K, if we adopt the dust temperature relationship of

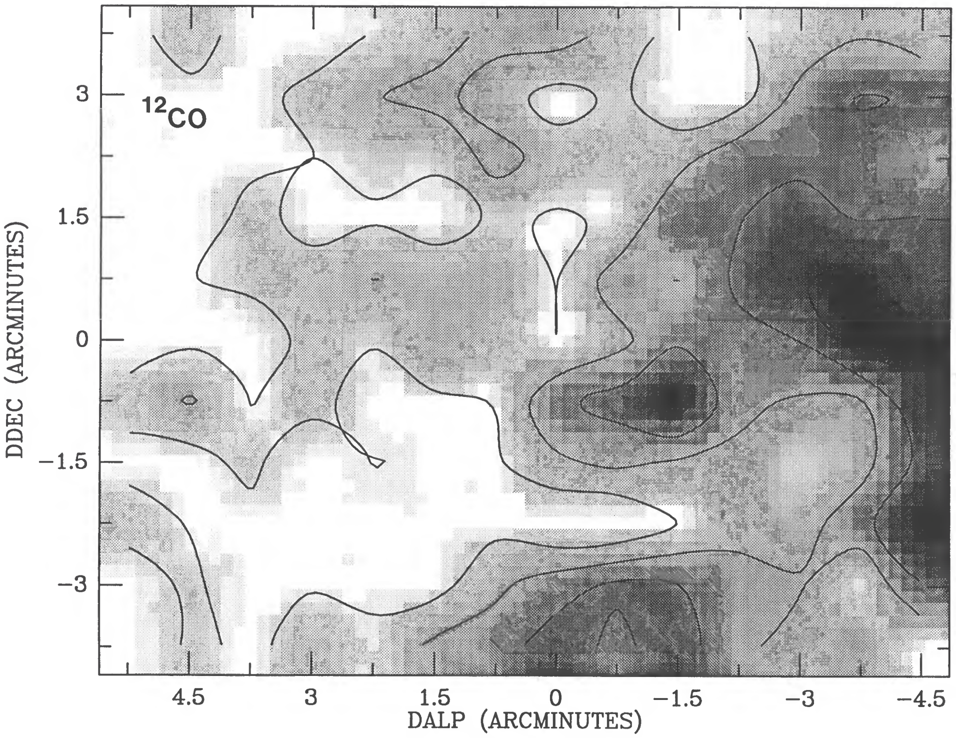

FIG. 1*a*

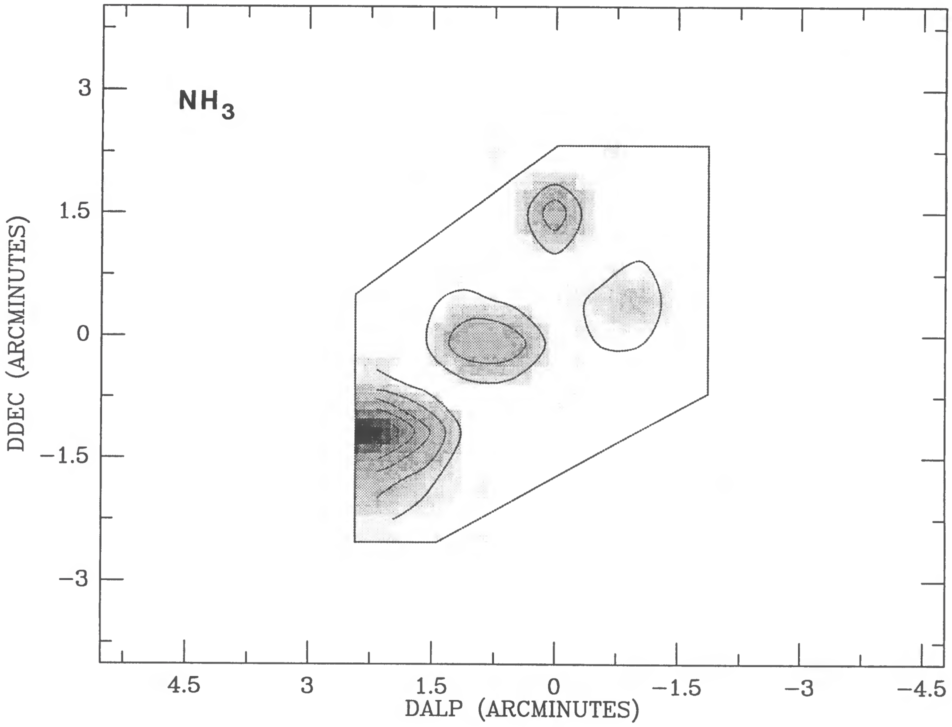

FIG. 1*b*

FIG. 1.—Distribution of peak intensity of ^{12}CO and NH$_3$ in NGC 2071(N). Offsets are relative to the nominal cloud center position $\alpha_{1950} = 05^{h}45^{m}00^{s}$, $\delta_{1950} = 00°39'00''$. (*a*) ^{12}CO $J = 1$–0 data from FCRAO giving the peak value of T_R^*. The lowest contour is 8.8 K, and the contour spacing is 0.4 K. (*b*) NH$_3$ (1, 1) data obtained with the Effelsberg antenna, from Iwata, Fukui, & Ogawa (1988), giving the peak antenna temperature corrected for beam efficiency; the lowest contour plotted is at the 0.9 K level, and the contour spacing is 0.45 K. The region covered by the data is indicated approximately by the dotted lines.

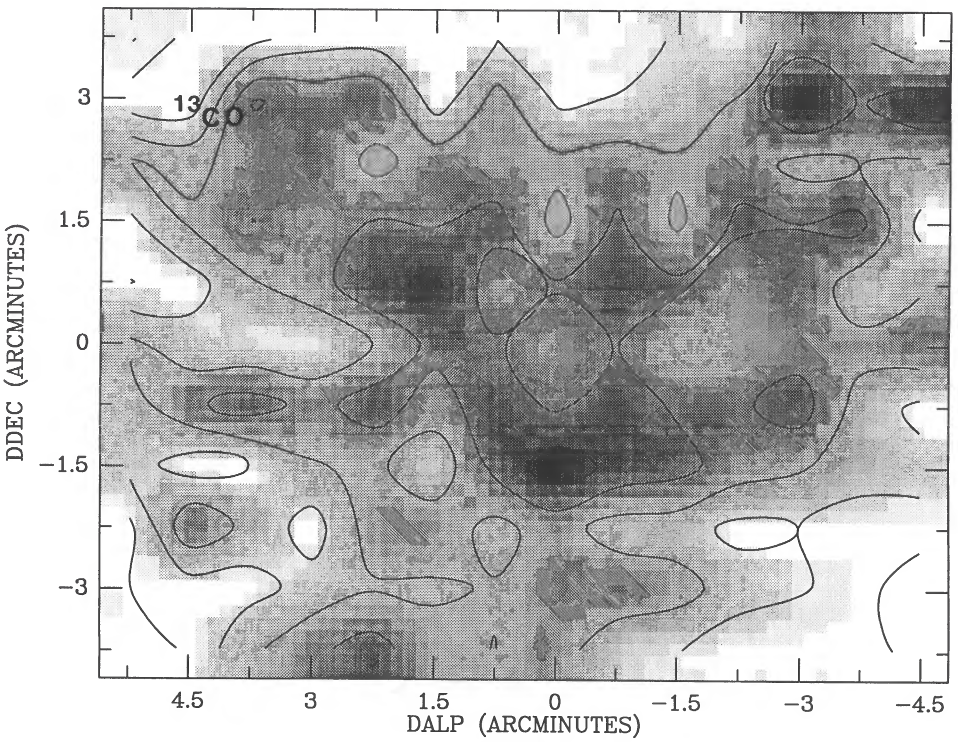

FIG. 2*a*

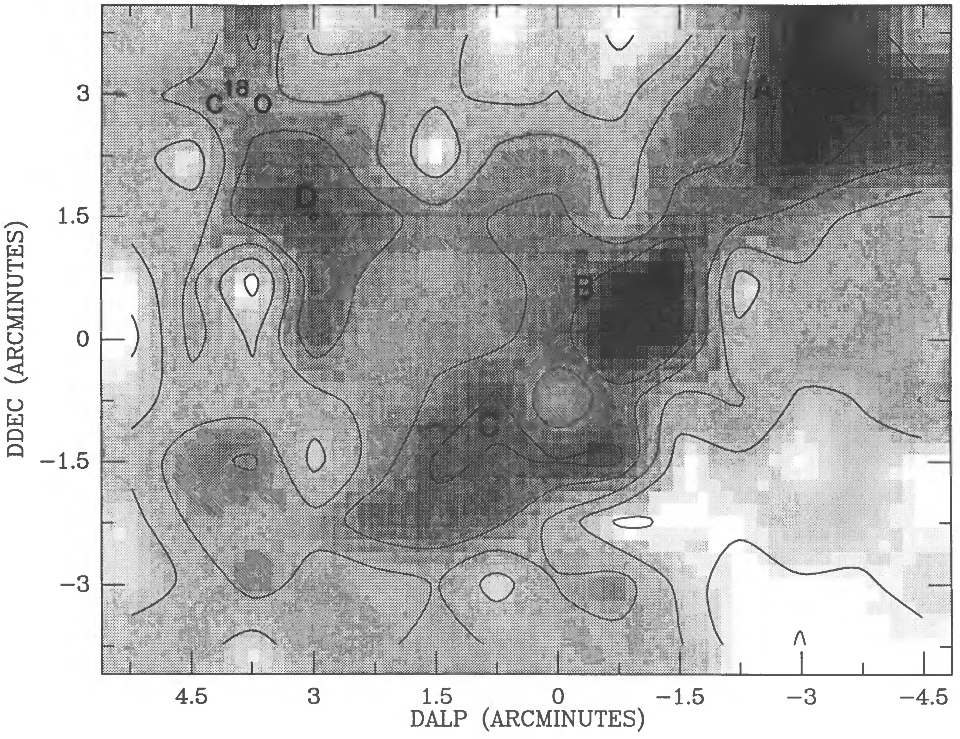

FIG. 2*b*

FIG. 2.—Maps of integrated emission of various species in NGC 2071(N). Map offsets are relative to nominal cloud center position as in Fig. 1. The integrals extend from 7 to 11 km s^{-1}, and observed antenna temperatures have been corrected for forward spillover and scattering to obtain T_R^*. (*a*) ^{13}CO $J = 1$–0; the lowest contour level is 7.0 K km s^{-1}, and the contour spacing is 1.8 K km s^{-1}. (*b*) C^{18}O $J = 1$–0; the lowest contour level and contour spacing are 0.45 K km s^{-1}. (*c*) CS $J = 2$–1; the lowest contour level and contour spacing are 0.36 K km s^{-1}. (*d*) HCO$^+$ $J = 1$–0; the lowest contour level and contour spacing are 0.39 K km s^{-1}. In this last species the area mapped was a rectangular region 6′ × 8′, somewhat smaller than that covered in the other lines observed at FCRAO.

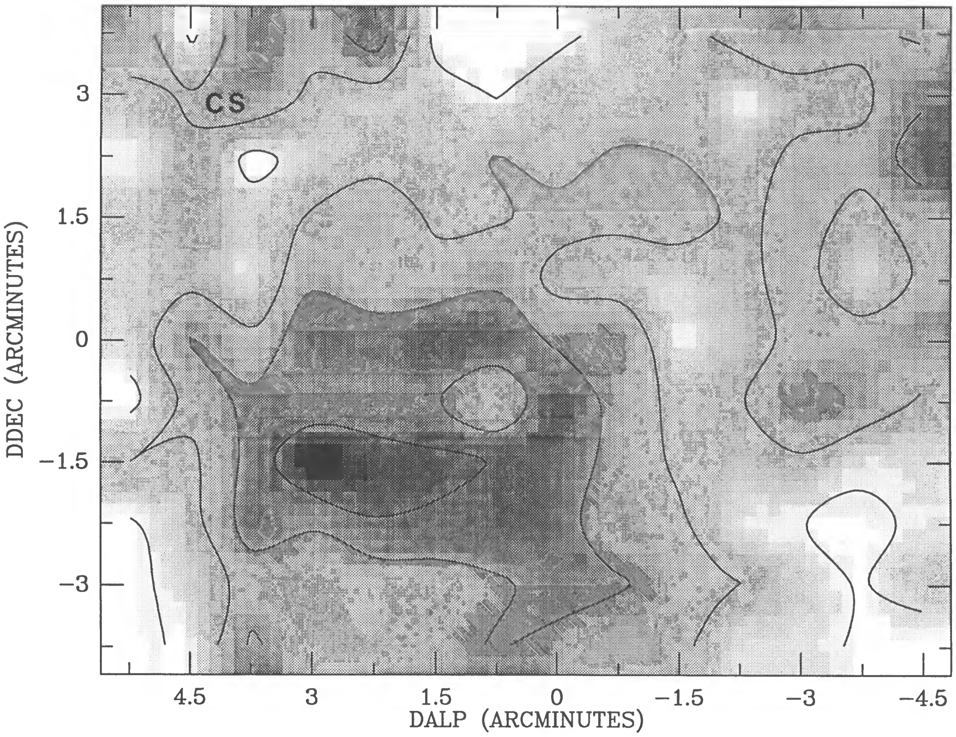
CS
3
1.5
0
−1.5
−3
DDEC (ARCMINUTES)
4.5
3
1.5
0
−1.5
−3
−4.5
DALP (ARCMINUTES)

FIG. 2*c*

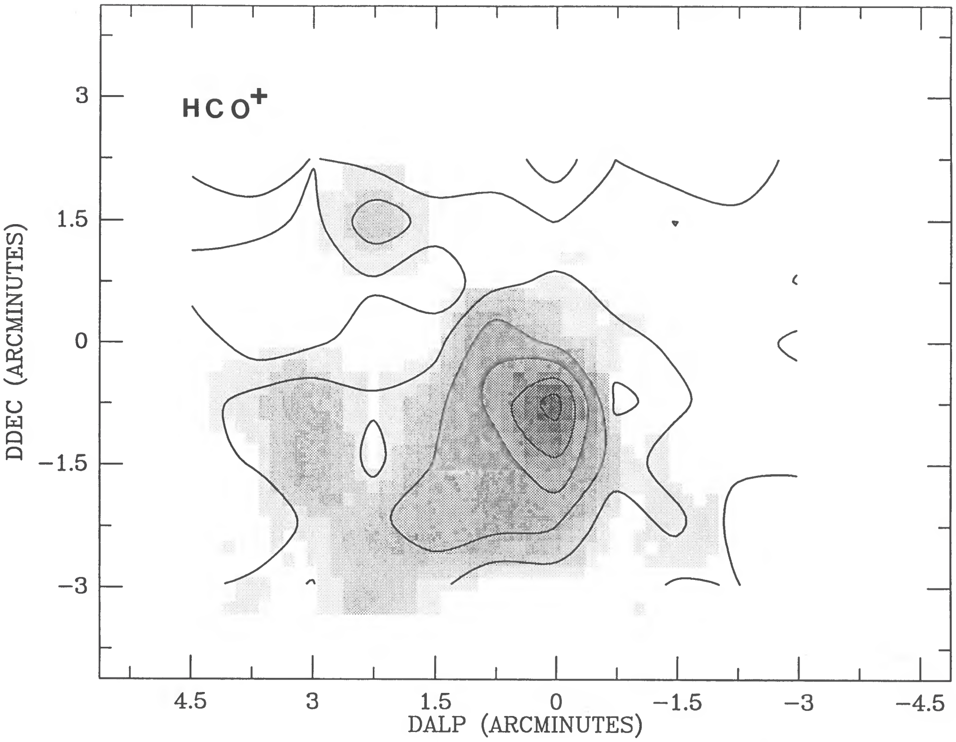
HCO+
3
1.5
0
−1.5
−3
DDEC (ARCMINUTES)
4.5
3
1.5
0
−1.5
−3
−4.5
DALP (ARCMINUTES)

FIG. 2*d*

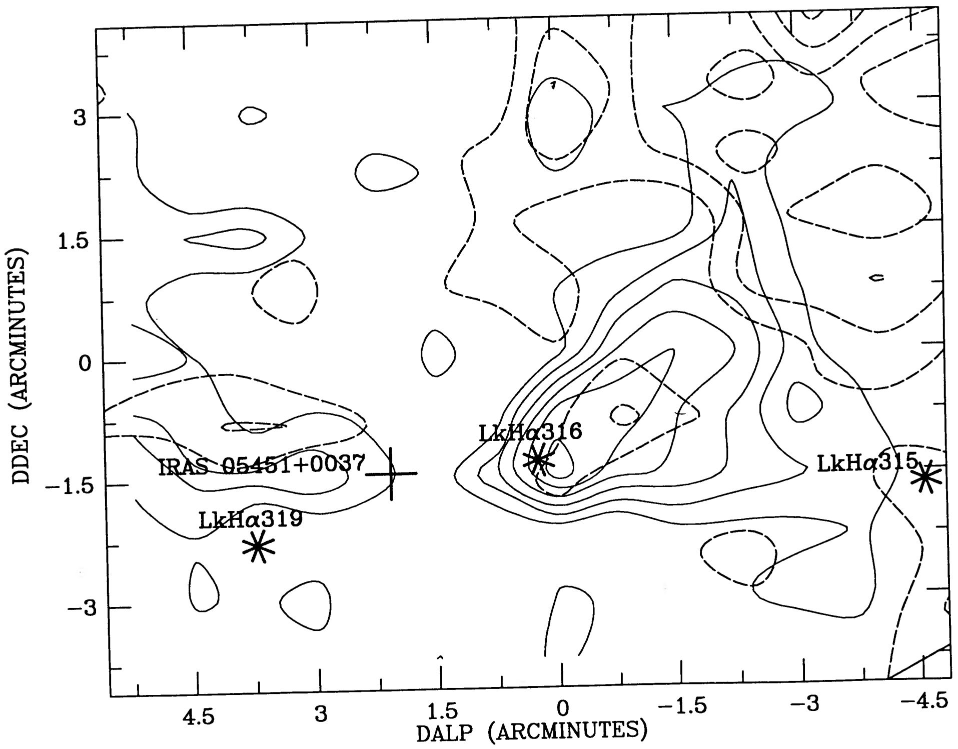

FIG. 3.—Map of high-velocity ^{12}CO $J = 1$–0 emission in NGC 2071(N). Map offsets are relative to nominal cloud center position as in Fig. 1. The solid lines are contours of redshifted emission integrated over the velocity range 11–15 km s^{-1}. The lowest contour level is 2 K km s^{-1}, and the contours are spaced by half this amount. The broken lines are the contours of blueshifted emission integrated over the velocity range 0–6 km s^{-1}; the lowest contour level is 2.5 K km s^{-1}, and the contours are spaced by 1.5 K km s^{-1}. The infrared source IRAS 05451+0037, denoted by the plus symbol, is nearly centrally located between the rather unequal lobes of high-velocity gas. The locations of three Hα emission T Tauri stars studied by Herbig & Kuhi (1963) are also indicated.

Scoville & Kwan (1976) and a dust absorption efficiency at 50 μm equal to 0.002 (Hildebrand 1983). The fact that we see no gas temperature enhancement as traced by the ^{12}CO peak temperature in this direction may be explained by the lack of sufficient density for the dust to heat the gas. For $T_{\rm dust} = 25$ K and $n = 10^4$ cm^{-3}, we find $T_{\rm gas} \simeq 12$ K, using the expressions for gas heating and cooling given by Goldsmith & Langer (1978). The densities in excess of 10^5 cm^{-3} required to closely couple $T_{\rm gas}$ and $T_{\rm dust}$ do not appear to be present in this region. This conclusion is supported by the analysis of CS emission given in § 4.

The ^{12}CO integrated emission (6–11 km s^{-1}) is essentially featureless, with the exception of a single enhanced region about 1.′5 in size centered at the (0, −1) position (all offsets are relative to the nominal cloud center position $\alpha_{1950} = 05^h45^m00^s$, $\delta_{1950} = 00°39'00''$), where the intensity rises to $\simeq 40$ K km s^{-1} compared with an average value of $\simeq 30$ K km s^{-1}. This position coincides with the location of the enhanced red- and blueshifted wings near LkHα 316. Since it does not coincide with any significant enhancement in the peak temperature, we attribute this peak in integrated intensity to the effect of wing emission in the velocity range characteristic of the quiescent cloud material.

3.2. ^{12}CO *High-Velocity Emission*

As seen in Figure 3, this emission is quite widespread throughout the region mapped. The morphology is complicated by the very extended blueshifted emission in the northeast; if we exclude this, we do see a distinct east-west structure approximately centered on IRAS 05451+0037. The bipolarity is confused by the presence of both red- and blueshifted emission to the east and west of the infrared source. This appearance can be explained, however, if we have a bipolar outflow whose axis lies essentially in the plane of the sky and which has nonzero expansion velocity perpendicular to its axis (Cabrit & Bertout 1986; Cabrit, Goldsmith, & Snell 1988). The somewhat complex structure of the high-velocity gas together with the requirement of good coverage to the east of the *IRAS* source explain why IRAS 05451+0037 is not clearly identifiable as the driving source of the outflow in the maps of IFO. Because of the limited signal-to-noise ratio and irregular geometry, as well as lack of information about optical depth and inclination, we have not attempted to calculate any detailed parameters of the bipolar outflow in NGC 2071(N).

3.3. ^{13}CO *Emission*

The distribution of integrated intensity in the $J = 1$–0 transition of ^{13}CO is shown in Figure 2*a*. As in the case of the ^{12}CO, we adopt a source coupling efficiency equal to unity. With the exception of its edges, the map has low contrast. There are several small, local maxima, having intensity 20%–40% greater than that of average of the region, excluding the northeast and southwest corners. The strongest peak at

---

[2] As discussed by IFO, IRAS 05451+0037 has no visible counterpart on POSS prints and is thus presumably deeply embedded in the molecular cloud. IFO used a distance of 500 pc for the NGC 2071(N) region. Our adoption of the 400 pc distance (Anthony-Twarog 1982) implies a reduction to 26 $L_{\odot}$. This does not have any significant effect on the calculations or interpretation.

(0, −1ʹ.5) coincides with the maximum in the ^{12}CO integrated intensity discussed above. The relatively low contrast is likely to result to a significant extent from the opacity of the ^{13}CO. The ratio of ^{12}CO to ^{13}CO peak temperatures is 2:1 over most of the central portion of the region studied, which with the usual assumptions of optically thick ^{12}CO emission and equal excitation temperatures for both isotopes, yields a ^{13}CO optical depth of 0.7. This relatively high opacity is presumably responsible for the reduced contrast of the ^{13}CO emission relative to the $C^{18}O$ emission (discussed below).

3.4. $C^{18}O$ *Emission*

As seen in Figure 2*b*, the $C^{18}O$ $J = 1–0$ emission has much higher contrast than the preceding species; in the map of the integrated intensity, the lowest contour level (which is at 3 times the rms noise level) is a factor of 6 lower than the highest values found. This is consistent with the $C^{18}O$ being optically thin (based on the ^{13}CO optical depth discussed above), so that the emission from this species should accurately trace its column density along the line of sight. This is reinforced by the maximum $C^{18}O$ intensity, which is only about 1.4 K, while regions with "strong" emission are characterized by $T_R^* \geq 1$ K. The line width varies considerably, but for the regions of strong emission it is 1.4–1.6 km s^{-1}. The $C^{18}O$ peak intensity map is quite similar to that of the integrated intensity of this species. There are at least four well-defined condensations in $C^{18}O$; these are discussed further in § 4.

3.5. CS *Emission*

The integrated CS $J = 2–1$ emission is shown in Figure 2*c*. The strong emission is concentrated in the region centered at (−1.5, +3.0), with the *IRAS* source being centered in the highest contour. The strongest peak emission in the map (with $T_R^* \geq 1$ K) is contained within the 1.08 K km s^{-1} contour of the integrated emission, suggesting that changes in line intensity rather than line width are responsible for the localized enhanced integrated intensity. The line width of the CS emission in this region is 1.7 km s^{-1}. The peak line emission shows a local minimum at the (+0.75, −0.75) position, as does the integrated emission shown in Figure 2*c*.

3.6. HCO^+ *Emission*

Figure 2*d* shows the integrated HCO^+ emission in NGC 2071(N) to be strongly concentrated around the (0, −0.75) position. This location coincides with a local minimum in the $C^{18}O$ emission, and is undistinguished in CS. It is essentially contained within the region of intense redshifted ^{12}CO emission (Fig. 3). The map of the maximum intensity of HCO^+ is not very different; although the position of greatest intensity is at (0, −1.5), its intensity there is only about 20% greater than at (0, −0.75). The diameter of the region (at half-maximum) is close to 2ʹ in both integrated and peak emission. The peak T_R^* is 1.3 K, and the FWHM line width is 1.1 km s^{-1}, similar to that found for CS and $C^{18}O$.

3.7. NH_3 *Emission*

The map of $(J, K) = (1, 1)$ ammonia emission shown in Figure 1*b* is taken from IFO, and gives the peak NH_3 emission. The data were obtained with the Effelsberg telescope having an angular resolution of 40ʺ. The region covered by the data is indicated approximately by the broken lines. The line widths do vary somewhat over the cloud, so that the integrated intensity distribution would be slightly different from the peak intensity distribution shown. The northernmost and southernmost clumps have slightly narrower line widths than the other two clumps ($\langle \Delta v \rangle = 0.75$ km s^{-1} compared with 1.15 km s^{-1}), and consequently would be relatively less emphasized in integrated intensity than shown here. This does not, however, significantly change the picture of the relative distribution of NH_3 in NGC 2071(N), which shows four clearly defined clumps within the central part of the region mapped in the millimeter lines. The westernmost clump is not fully mapped, but it is very nearly coincident with the *IRAS* source. Ammonia was observed toward the *IRAS* source in NGC 2071(N) by Wouterloot, Walmsley, & Henkel (1988) in the (1, 1) transition, and an upper limit was obtained for the (2, 2) transition. Using a kinetic temperature of 14 K, they derived a column density of 7×10^{14} cm^{-2}.

3.8. *Other Species*

We searched for other molecular lines that might delineate the dense gas in this region. The HCN $J = 1–0$ transition was detected in a number of positions near the center of the cloud, but its maximum intensity over the region which included peaks in all of the other species mapped was only a few times 0.1 K, precluding useful analysis of its distribution. The $J = 9–8$ transition of HC_3N was also sought at several positions corresponding to the peaks of other molecules, but no detection was made to a limit of 0.1 K rms.

4. DISCUSSION

The central point of this project is the study of the relationship of the small-scale morphology seen in different tracers to the chemistry of dense molecular clouds and to our ability to determine their structure. With limited data at our disposal, we have to make reasonable assumptions about the information in each of the spectral lines and maps that we have obtained.

4.1. *Analysis of Emission from Different Molecular Species*

The first assumption is that the emission from $C^{18}O$, CS, NH_3, and HCO^+ can be treated as optically thin. There are admittedly concerns, particularly about the optical depth of the CS and HCO^+. The weakness of the lines, and the fact that we are using only the integrated intensities (which include material in the line wings which is plausibly thin even if the center of line is saturated) suggest that the linear relationship between integrated intensity and column density is unlikely to be much in error. The observations of CS and nondetections of $C^{34}S$ in a number of dense cores by Zhou et al. (1989) are consistent with the peak CS optical depth not being very much larger than unity. It is also the case that if the lines observed are weak in the sense of $T_R < h\nu/k$, which is the case for the CS and $C^{18}O$ lines, and the emission is assumed to fill the beam, then the intensity is proportional to the column density of the molecular species, even if the optical depth exceeds unity (Penzias 1975; Linke et al. 1977).

The major problem in determining the relative distribution of various species is unraveling the problems of excitation and molecular column densities. Even with the assumption of optical thinness, this is not straightforward, owing to the differing excitation requirements and level structures of commonly studied traces. The spontaneous emission coefficients and frequencies of the transitions we have observed are given in Table 2; although the frequencies are mostly quite close, the Einstein *A*-coefficients span almost three orders of magnitude. We shall divide the problem into two parts, the first of which is deter-

TABLE 2

A-COEFFICIENTS AND FREQUENCIES FOR OBSERVED TRANSITIONS

Molecule	Transition	*A*-Coefficient (s^{-1})	Temperature ($\Delta E/k$, K)
$C^{18}O$	$J = 1$–0	6.5×10^{-8}	5.3
CS	$J = 2$–1	1.8×10^{-5}	4.7
HCO^+	$J = 1$–0	4.6×10^{-5}	4.3
NH_3	$(J, K) = (1, 1)$	1.7×10^{-7}	1.1

TABLE 3

CRITICAL DENSITIES FOR COLUMN DENSITY DETERMINATION FROM OBSERVED TRANSITIONS[a]

Molecular Transition	n_{cr} (cm^{-3})	x_0	n_0 (cm^{-3})
$C^{18}O$ $J = 1$–0	1.1×10^3	0.26	2.8×10^2
CS $J = 2$–1	4.7×10^5	0.33	1.6×10^5
HCO^+ $J = 1$–0	2.0×10^5	0.39	8.0×10^4
NH_3 $(J, K) = (1, 1)$	2.0×10^3	2.93	5.9×10^3

[a] Collision rate coefficients for kinetic temperature of 20 K taken from Green & Chapman 1978 for CS and $C^{18}O$ scaled by factor of 1.5 as described in text. Collision rate coefficient for HCO^+ from Monteiro 1985, and for NH_3 from Danby et al. 1988. The background temperature is taken to be 2.8 K.

mining the column density of the upper level of the observed transition, and the second is determining the total molecular column density.

The integrated antenna temperature from an optically thin transition is proportional to the column density of the upper level, but the coefficient of proportionality depends on a complex manner on the degree of excitation. In general we may write

$$(8\pi k \nu^2/hc^3) \int T_r\, dv = A_{ul} N_u \Gamma \,, \tag{1}$$

where $\int T_r\, dv$ is the line excess radiation temperature (antenna temperature corrected for atmospheric absorption and coupling efficiency) integrated over velocity (in K cm s^{-1}), A_{ul} is the spontaneous emission coefficient, N_u is the upper-level column density (cm^{-2}), and Γ is a correction factor, which is given by

$$\Gamma = 1 - \{[\exp(h\nu/kT_{ex}) - 1]/[\exp(h\nu/kT_{bg}) - 1]\} \,. \tag{2}$$

In this expression, T_{ex} is the excitation temperature relating the upper and lower level molecular populations, and T_{bg} is the temperature of the isotropic blackbody background radiation. If we treat the excitation of the observed transition as a two-level problem, we can obtain Γ as an explicit function of the excitation rate (cf. Linke et al. 1977):

$$\Gamma = x[1 - g(K - 1)]/(gK + x) \,, \tag{3}$$

where

$$x = C_{ul}/A_{ul} = n(H_2)/n_{cr} \tag{4a}$$

and

$$n_{cr} = A_{ul}/\langle \sigma v_{ul} \rangle \tag{4b}$$

is the "critical density" for which downward collision and spontaneous emission rates are equal. We have also defined

$$g = [\exp(h\nu/kT_{bg}) - 1]^{-1} \tag{4c}$$

and

$$K = \exp(h\nu/kT_{ex}) \,. \tag{4d}$$

For $g \neq 0$, the value of Γ is extremely small at low densities ($x \ll gK$). This is because most of the population of the upper level is due to the background radiation rather than to the collisional excitation, and consequently the line emission above the background reflects only a very small fraction of the total upper-level column density. We define x_0 by the requirement that Γ for $x = x_0$ be equal to 0.5. This yields

$$x_0 = gK/[1 - 2g(K - 1)] \,. \tag{5}$$

We define a critical density for having the integrated line temperature trace the upper-level column density by

$$n_0 = x_0 A_{ul}/\langle \sigma v_{ul} \rangle \,. \tag{6}$$

For densities greater than n_0 (in terms of eq. [2]: $T_{ex} \gg T_{bg}$), the integrated line intensity is within a factor of 2 of being proportional to the upper-level column density, and we can say that *$\int T\, dv$ does trace N_u irrespective of the local density along the line of sight*. For lower densities this is not the case, and the emission depends on the local density as well as the column density of the species being observed.

An important reason for separating the excitation issue into the determination of Γ and F_u (the fraction of the population in the upper level of the observed transition) is that for some species, particularly $C^{18}O$, the density in the central region of NGC 2071(N) is likely to be greater than n_0. Thus, the $C^{18}O$ integrated intensity should be a reasonably good tracer of the upper-level column density. Values of x_0 and n_0 from equations (5) and (6) are tabulated in Table 3.

The value of n_0 for NH_3 exceeds that for $C^{18}O$ by a factor $\simeq 20$, considerably more than the ratio of the *A*-coefficients. The difference is due to the much larger value of x_0 arising from the lower frequency of this transition. Thus we see that the NH_3 emission maps the upper-level column density of this species only in relatively denser regions. Note that $n_0(HCO^+)$ is approximately half that of CS $J = 2$–1, although its *A*-coefficient is about 2.5 times larger; this is a result of the larger collision rate coefficients for the molecular ion. We cannot expect the emission from CS and HCO^+ to trace the upper-level column density of the observed transitions. However, the relatively similar values of n_0 suggest that excitation processes should not produce a significant *differential* effect in the weighting of emission by the local H_2 density.

The total molecular column density N and upper-level column density N_u are related by the upper-level fraction F_u through

$$N_u = F_u N \,. \tag{7}$$

Despite the fact that the upper-level fraction can be computed only by solving a multilevel statistical equilibrium problem, it appears that uncertainties in this quantity are a much smaller source of uncertainty than those in Γ. We have computed F_u for the $J = 1$ level of $C^{18}O$ and the $J = 2$ level of CS, appropriate to the transitions of these species that we have observed in NGC 2071(N). The results as a function of hydrogen density and kinetic temperature are shown in Figure 4. For both species we have adopted the excitation rates of Green & Chapman (1978), scaled by a factor of 1.5 to account for H_2 rather than He collisions. Despite the different levels being considered, the behavior is qualitatively similar, in that for a given kinetic temperature F_u is small for low densities,

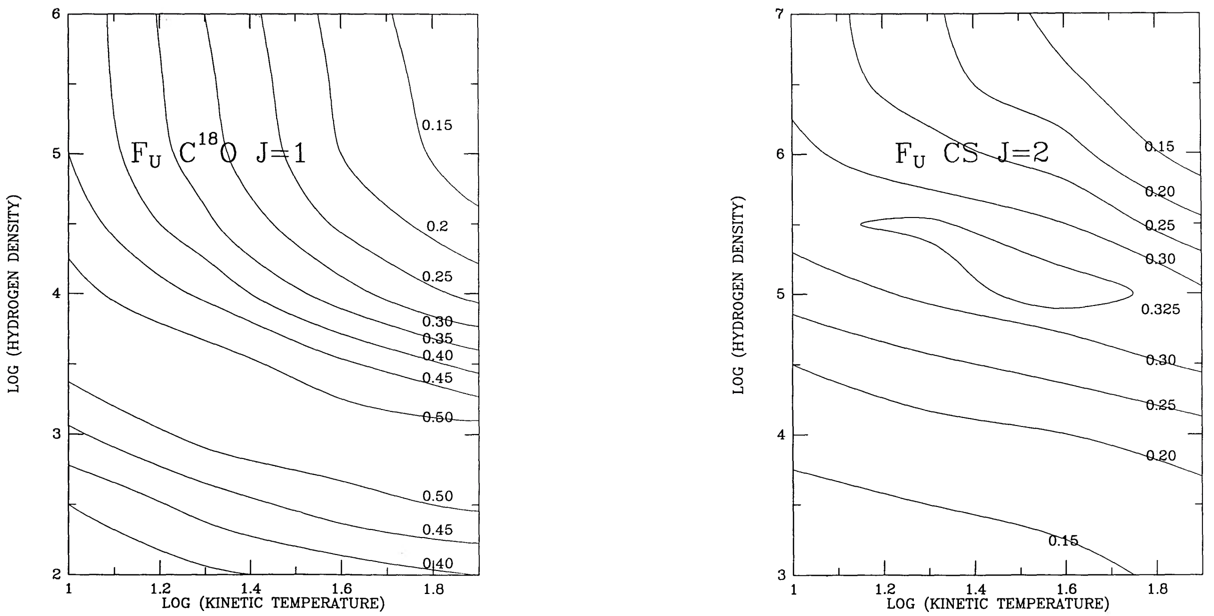

FIG. 4*a*

FIG. 4*b*

FIG. 4.—Fraction of molecular population (*a*) in the $J = 1$ level of $C^{18}O$ and (*b*) in the $J = 2$ level of CS. The isofractional curves are obtained by solving equations of statistical equilibrium assuming that all transitions are optically thin.

increases as $n(H_2)$ is increased, and then drops again at higher densities.

There is a characteristic molecular hydrogen density, which we shall call n_{max}, that *maximizes* F_u in each case; this density is approximately a factor of 300 higher for CS than for $C^{18}O$. The turn-up of the curves in Figure 4 for high densities reflects the attainment of LTE; note that for this to be reflected in F_u we must have thermalized all levels which have significant population at the kinetic temperature in question. The value of n_{max} is a weakly declining function of the kinetic temperature over the 10–80 K range considered here. For CS $J = 2$, for example, n_{max} diminishes from 3×10^5 cm^{-3} to just below 1×10^5 cm^{-3} over this range of kinetic temperature.

The value of displaying the fractional populations in Figure 4 is that we can gain an idea (from inspection of the curves) of the magnitude of the changes in relationship between column density and antenna temperature produced by variations in physical conditions. The range for these particular upper levels is surprisingly small. The value of F_u for CS $J = 2$ does not drop below 0.14 under any combination of $n(H_2) \leq n_{max}$ and kinetic temperature, and it only drops this low at high densities for $n(H_2) > 3 \times 10^6$ cm^{-3} and $T_{kin} > 60$ K, extremes which seem unlikely to occur over a significant fraction of this not extremely active region. Since the maximum value of F_u is 0.325, the fraction of population in the $J = 2$ transition of CS is constrained to within less than a factor of 2. In the sense of not being overly sensitive to physical conditions, the $J = 2$–1 transition is an extremely fortuitous choice, since under a wide range of conditions in fairly quiescent clouds it contains a fairly large fraction of the total CS column density.

We would expect the behavior for HCO^+ to be qualitatively similar, but with appropriately different value of n_{max}. For NH_3, the upper level of the (1, 1) inversion doublet is so close to the ground state ($\Delta E/k = 1.1$ K) that the fraction of population in the upper level for very low excitation is relatively large, on the order of 0.5, and declines to quite low values in LTE. Thus, there is a somewhat larger range of values of F_u than for the higher frequency lines. For all species we have observed except for $C^{18}O$, the uncertainty in F_u is far exceeded by that in Γ, which, as discussed above, can range downward from $\simeq 1$ for LTE to arbitrarily small values for highly subthermal excitation.

4.2. $C^{18}O$ *Emission and Clumps in Column Density Distribution*

$C^{18}O$ is the only species we have observed for which we are confident that $n(H_2) > n_0$ and $\Gamma \cong 1$, so that we can directly determine the upper-level column density along the line of sight from the integrated line intensity. For this molecule we adopt a coupling efficiency of 0.76 ($\eta_c = \eta_b/\eta_{fss} = 0.55/0.72$) in view of the relatively fragmented emission in this species, and obtain

$$N(C^{18}O) = 4.7 \times 10^{14} \int T^*_{R\,J=1-0}\,dv/F_{J=1}\ \mathrm{cm}^{-2}\,, \qquad (8)$$

where the integrated intensity has units of K km s^{-1}. The emission shown in Figure 2*a* is obviously very uneven, and the clump densities derived below are on the order of 10^4 cm^{-3}. We do not know how much of the emission is due to the clumps and how much to the interclump gas, so that the value of F_u we use is uncertain. We adopt 0.4 as a compromise between clump and interclump material, although, as discussed above, there is relatively little sensitivity to physical conditions.

For the analysis of the $C^{18}O$ emission we adopt a uniform fractional abundance relative to H_2 of $X(C^{18}O) = 1.7 \times 10^{-7}$ (Frerking, Langer, & Wilson 1982). The data of Figure 2*b* do not convincingly show that we have mapped the full extent of the $C^{18}O$ emission, but within the region mapped the average integrated intensity is 1.33 K km s^{-1}. The total mass is equal to 180 $M_{\odot}$, and the average molecular hydrogen density,

1992ApJ...385..522G

assuming a cloud line-of-sight size equal to its characteristic transverse dimension of 10′ (1.17 pc), is 2.6×10^3 cm^{-3}. This relatively high value justifies our adoption of $\Gamma = 1$ for C^{18}O.

In order to discuss the clumpiness traced by C^{18}O, it seems appropriate to adopt methods for distinguishing a "clump" from the more diffuse emission that characterizes most of the central regions of clouds such as NGC 2071(N). These definitions will necessarily be somewhat arbitrary and imprecise, but having such criteria will at least make it clear how we define a dense condensation from the surrounding material. The four criteria that we have adopted to define a clump are the following:

1. Peak emission must be 3 σ or more above the local background.
2. Peak emission must be 50% or more above average over the map.
3. Clump emission must be simply connected.
4. Clump must be extended in antenna beam used for the observations.

Based on these criteria, there are four clumps defined by the C^{18}O emission. We consider the clumps to be regions of excess emission relative to an extended background having dimensions considerably smaller than those of the dense core of the cloud. The area of a clump is the region (in 45″ pixels) over which the emission exceeds the half-power level; the latter is taken as the average emission over the cloud plus one-half of the difference between the peak clump emission and that of the surrounding background. The total mass of each clump is computed from the sum of the excess column densities. The average clump densities are determined from the clump masses with the assumption of spherical geometry. With the above simplifications, we obtain the clump characteristics given in Table 4.

We have also computed the virial mass for each clump, assuming that gravity alone is balancing the apparent line width and an r^{-1} density law, using the expression given by MacLaren, Richardson, & Wolfendale (1988). It is immediately apparent that the clumps traced by C^{18}O comprise only a small fraction of the mass of the dense core of NGC 2071(N). Their mean internal density is approximately an order of magnitude greater than that of the interclump material. This large contrast justifies the neglect of external pressure in evaluating the virial equation, and from the large discrepancy between actual and virial masses we conclude that the clumps are unbound. This is in distinction to the core as a whole, for which the observed and virial masses (again computed assuming an r^{-1} density law) agree within 50%.

4.3. *Comparison of Distribution of Various Species*

To facilitate comparison of the distribution of different molecular species, we have combined representative contours highlighting the regions of strong emission in C^{18}O, NH$_3$, HCO$^+$, and CS in Figure 5.

4.3.1. C^{18}O *and* ^{13}CO *Clumps*

The ^{13}CO $J = 1$–0 transition should have $\Gamma \cong 1$, but, as discussed in § 3.2, the emission from this species is relatively uniform, presumably as a result of its high optical depth (≥ 1). Thus, it is doubtful whether the ^{13}CO emission is a faithful tracer of column density. As can be seen by comparing Figures 2*a* and 2*b*, the C^{18}O and ^{13}CO maps appear quite different. There is a local maximum in the ^{13}CO emission concident with clump A in C^{18}O, and another ^{13}CO maximum just adjacent to clump C, coincident with LkHα 316. Neither C^{18}O nor ^{13}CO has a maximum at the position of IRAS 0541+0037, although there is emission from both these species there. Unless there has been a significant reduction in the fractional abundance of C^{18}O, we must conclude that the formation of this infrared source has occurred without a noticeable enhancement of the column density as measured by this relatively unbiased tracer, or that the core material has already been dispersed.

4.3.2. NH$_3$ *Emission*

The value of n_0 for the NH$_3$ (1, 1) inversion transition is, as seen in Table 3, significantly higher than for C^{18}O $J = 1$–0. From the density determinations from C^{18}O given above, the general core density of 2.6×10^3 cm^{-3} is less than a factor of 3 below n_0(NH$_3$). The density in the clumps defined by C^{18}O (Table 4) considerably exceeds this density, with the result that the ammonia emission per molecule along the line of sight from the general core material will be somewhat weaker than for emission from denser clump regions.

The region mapped in NH$_3$ includes only two of the C^{18}O clumps; B coincides with one of the peaks in NH$_3$, but clump C shows *no* significant ammonia emission. In addition, there are three ammonia maxima which *do not* agree in position with local maxima of C^{18}O. The most significant of these is the strongest NH$_3$ peak, which is approximately centered on the *IRAS* source 05451+0037. While we do not know the density in this region with certainty, it is plausibly (5–10) $\times 10^3$ cm^{-3}, sufficient to make Γ(NH$_3$) fairly close to unity. This is only slightly larger than the average core density, so that it is unlikely that the very strong ammonia emission near the *IRAS* source is entirely due to a density enhancement, and since we do not see evidence for a column density peak there, the most

TABLE 4

CLUMP PROPERTIES IN NGC 2071(N) FROM C^{18}O EMISSION

Clump	Center[a]	Δv[b] (km s^{-1})	Size[c] (pc)	Peak N(H$_2$) (10^{22} cm^{-2})	$\bar{n}$ (10^4 cm^{-3})	Mass[d] ($M_\odot$)	$M_{\rm vir}$[e] ($M_\odot$)
A	(−3.5, +3.0)	1.53	0.23	2.0	2.2	6.3	51
B	(−1.0, +0.5)	1.74	0.21	2.2	2.4	5.8	60
C	(+0.75, −1.25)	1.85	0.25	1.8	1.5	6.1	81
D	(+3.0, +1.5)	1.47	0.23	1.8	1.4	4.6	47

[a] Offsets in minutes of arc relative to map center position.

[b] Full width to half-maximum line width averaged over pixels comprising clump.

[c] Size taken to be (clump area)$^{0.5}$.

[d] Mass calculated from excess column density.

[e] Virial mass obtained from average line width and clump size.

1992ApJ...385..522G

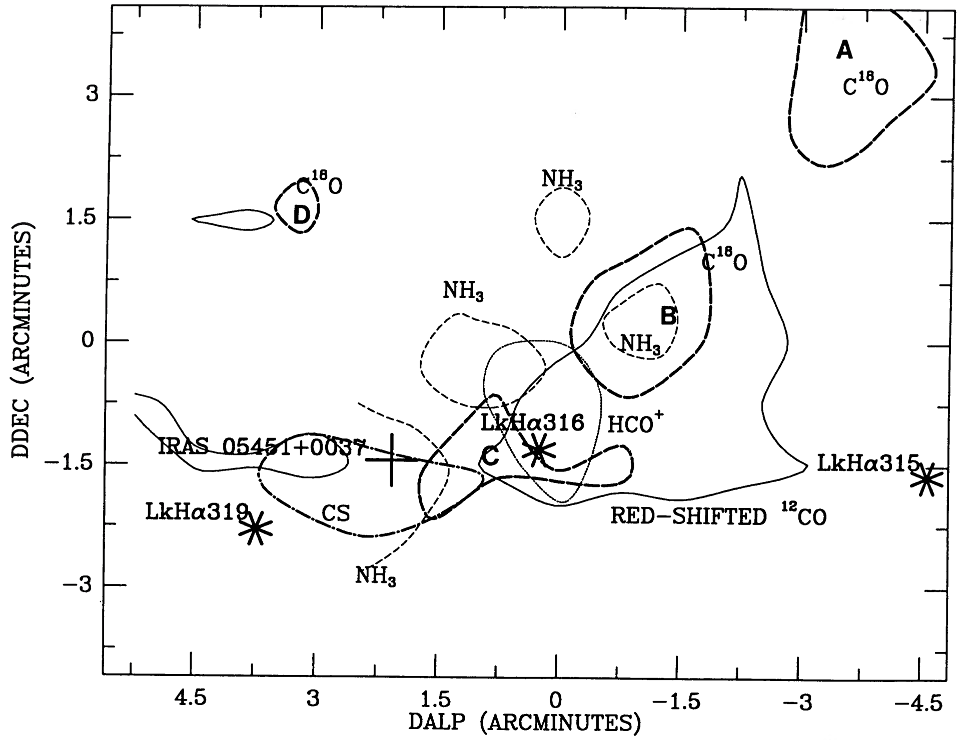

FIG. 5.—Composite view of peaks in emission of C^{18}O (2.2 K km s^{-1}; *heavy broken line*), CS (1.44 K km s^{-1}; *dash-dot line*), NH$_3$ (0.9 K; *light broken line*), and HCO$^+$ (1.95 K km s^{-1}; *dotted line*) molecular emission, all within the quiescent cloud velocity range, and the redshifted high-velocity ^{12}CO emission (3 K km s^{-1}; *light solid line*). Map offsets are relative to nominal cloud center position as in Fig. 1. The locations of the *IRAS* source and the three Hα emission stars located within the region mapped are also indicated.

likely explanation is that the fractional abundance of NH$_3$ has significantly increased. From the NH$_3$ column density determined by Wouterloot et al. (1988), an assumed size of the NH$_3$ clump of 2′, and taking the hydrogen density there to be 3×10^3 cm^{-3}, we determine an NH$_3$ fractional abundance equal to 2.7×10^{-7}. This is indeed on the high end of giant molecular cloud results (Irvine, Goldsmith, & Hjalmarson (1987), and a factor $\cong 3$ higher than found in the dark clouds B1 (Bachiller, Menten, & del Rio-Alvarez 1990), TMC-1 (Guélin 1988), and other dark clouds (Benson & Myers 1983).

The ratio of NH$_3$ intensity to C^{18}O integrated emission at peak B is 0.5, while at peak C it is 0.3. At the ammonia maximum coincident with the *IRAS* source the ratio is 2.2; at the two other NH$_3$ peaks not associated with C^{18}O maxima, it is approximately unity. Assuming that the C^{18}O and NH$_3$ emission do trace total column densities of these species, the change in their relative fractional abundance is approximately a factor of 5 between different maxima within the core of NGC 2071(N).

4.3.3. CS *and* HCO$^+$ *Emission*

As discussed in § 3.5 and shown in Figure 2*c*, the CS emission has a single strong peak which coincides with the location of the *IRAS* source. The value of n_0 for CS $J = 2$–1 emission (Table 3) is the largest of any of the spectral lines observed in this study. Its emission almost certainly arises from a region with $n(\mathrm{H_2}) < n_0$, since it is otherwise difficult to see how we could avoid seeing a local maximum in the C^{18}O emission. In the limit $x \ll 1$, equation (1) becomes

$$(8\pi k\nu^2/hc^3)\int T_r\,dv = N_u\,n(\mathrm{H_2})\langle\sigma v\rangle[1 - g(K-1)]/gK\ , \quad (9)$$

recalling the fact that for highly subthermal lines the emission is proportional to the column density in the upper level times the collision rate. For CS $J = 2$–1, we obtain the relationship

$$N_u(\mathrm{cm^{-3}}) = [1.52 \times 10^{17}/n(\mathrm{H_2})]\int T_r\,dv\ \mathrm{K\ km\ s^{-1}}\ . \quad (10)$$

Taking $F_u = 0.25$ and a line-of-sight dimension for the emitting region equal to 0.175 pc (1′.5), we obtain a fractional abundance $X(\mathrm{CS}) = N(\mathrm{CS})/N(\mathrm{H_2}) = 1.9 \times 10^{-8}$ for a density of 10^4 cm^{-3}.

This density together with the clump size would produce a C^{18}O integrated intensity of 0.8 K km s^{-1}, approximately a factor of 2 greater than the limit for any clump excess emission at this position. This CS fractional abundance is larger than typically determined for interstellar clouds [$(0.4$–$1) \times 10^{-8}$; Irvine et al. 1987]. That the abundance of CS may vary considerably is indicated by the study of NGC 2071 by Zhou et al. (1991), who find a value of X(CS) equal to 0.2×10^{-8}. The low H$_2$ density required to avoid having the molecular column density associated with the *IRAS* source produce detectable excess C^{18}O emission thus requires a significant increase in the fractional abundance of CS in the vicinity of the young star.

The strong HCO$^+$ emission shown in Figure 2*d* is also very confined, but peaks at an entirely different location. As seen clearly by comparison with Figure 3, the HCO$^+$ is concentrated in the region of most intense redshifted ^{12}CO emission, which is also where blueshifted emission overlapping the lobe of the redshifted gas is located. This may highlight the region where the outflow is impacting the surrounding molecular material, and is clearly having a major effect on its chemical composition. Using the same parameters for clump C associated with the *IRAS* source given above, we find the fractional abundance for HCO^+ there to be 2×10^{-9}. The lack of information about physical conditions in the region where emission from this species peaks makes abundance determination there difficult, but it is almost certainly an order of magnitude higher. The idea that we are seeing the impact of the shock is supported by the 10.2 km s^{-1} peak velocity of the HCO^+ line, which is considerably redshifted relative to the 8.7–9.3 km s^{-1} range characterizing the CS and $C^{18}O$ emission from all the condensations in these tracers. The line width of the HCO^+ emission in the region of strong emission is ≈ 1.1 km s^{-1}, somewhat narrower than the line width characterizing the $C^{18}O$ and CS emission. The relatively narrow width of the HCO^+ spectra is a characteristic shared with the emission from this species in small clumps in the HH 7–11 region studied by Rudolph & Welch (1988). However, the larger velocity shift of the HCO^+ relative to the ambient cloud velocity seen here compared with HH 7–11, as well as the greater line width in this species (1.2 km s^{-1} compared with 0.5 km s^{-1}), suggests a somewhat different situation from that found for the HH 7–11 clumps, which are quiescent and essentially at rest with respect to the ambient material. The process producing the enhancement in the abundance of HCO^+ in NGC 2071(N) is apparently very selective, with the HCO^+ abundance increased only in a kinematically very limited region which has been accelerated by the outflow.

4.4. *Chemistry Driven by the Outflow in NGC 2071(N)*

The material in the NGC 2071(N) region appears relatively fragmented in the lines of the various molecules we have observed. The distribution of material as indicated by the different tracers appears rather more dissimilar than similar. This is particularly striking when the maps of $C^{18}O$, CS, and NH_3—three widely used molecular probes—are compared. Taking $C^{18}O$ as the least biased in terms of sensitivity to local density and a molecular species which is likely to have a fairly constant fractional abundance, we find that the clumps suggested by the local maxima in the $J = 1$–0 transition of this species are unbound. The *IRAS* source 05451+0037 appears to be the driving source of a molecular outflow which is comparable in extent to the region over which we see the clumps in the more quiescent material.

The combination of the above suggests that we should consider the chemical differentiation that we observe to be the result of time-dependent chemistry occurring in instabilities driven by the outflow. This specific scenario has been suggested by Goldsmith et al. (1986), and developed in some detail by Charnley & Williams (1990) and Charnley et al. (1990). The latter two papers deal with the chemical evolution of a preexisting cold, dense clump [$T = 10$ K; $n(H_2) = 7 \times 10^3$ cm^{-3}] as a result of the passage of a shock wave driven by the wind from a young star. The shock increases the abundance of HCO^+ by a factor $\cong 10^3$ within approximately 10^3 yr after the passage of the shock, while the abundance of CS is either unaffected or, in some models, can be significantly reduced for a period of a few thousand years. The abundance of CO is largely unaffected, but can under certain conditions be reduced by an order of magnitude for times of $10^{4.5}$ yr or more. Note that the increase in HCO^+ abundance predicted by Charnley et al. (1990) is a change in the opposite sense from that predicted by Mitchell & Deveau (1982; 1983).

It is difficult to make any direct comparison between the chemical calculations that have been carried out and our observations, except in the most general sense. The limited quantitative information we have obtained is presented in Table 5, together with some of the results of shock chemistry calculations. The CS abundance is far less than the equilibrium, and somewhat below than the postshock values predicted by Charnley et al. However, the increase in CS abundance that we require in order to explain having the emission from this species restricted to the vicinity of IRAS 05451+0037 directly conflicts with the Charnley et al. models in which the CS abundance is *reduced* by the passage of the shock. The HCO^+ abundance is obviously in reasonable agreement with the Charnley et al. (1990) model, especially recalling that at its peak, the HCO^+ fractional abundance is an order of magnitude higher than the values given in Table 5 for clump C. The enhancement in HCO^+ abundance is definitely spatially separated from the *IRAS* source, implying a significantly different time scale, if this effect is connected with a shock or wind produced by the young stellar object.

TABLE 5

RESULTS OF MODELS OF CHEMISTRY IN SHOCKS AND COMPARISON WITH DATA FOR CLUMP C

MOLECULE	MEASURED ABUNDANCE[a]	MODELED ABUNDANCE	
		Postshock	Other
CS	1.9×10^{-8}	5.0×10^{-8}	1.9×10^{-7}[b]
HCO^+	2.0×10^{-9}	4.0×10^{-7}	2.2×10^{-9}[b]
HCO^+	...	4.7×10^{-13}	8.0×10^{-11}[c]
NH_3............	2.7×10^{-7}	2.0×10^{-6}	1.1×10^{-8}[c]

[a] Relative to H_2.

[b] From Charnley et al. 1990 model 3 after 3×10^3 yr compared with equilibrium abundance.

[c] From Mitchell & Deveau 1982 compared with preshock abundance.

It is also the case that the clumps may themselves be a result of instabilities produced by the outflow, and the dynamical and the chemical evolution of the material in the vicinity of an outflow are closely coupled. For example, the abundance of H_2O, which is an extremely effective coolant of molecular material in the 25° to few hundred degree range, is enhanced by up to a factor of 100 in the models of Charnley et al. Thus, the changes in molecular composition in the surrounding material produced by the stellar wind and outflow may be very significant for its subsequent evolution and possible star formation activity.

In the case of NGC 2071(N), the $C^{18}O$ "clumps" which we have found to be unbound may be essentially transient structures, which are largely the result of compression of the general cloud core material. The impact of the shock has significantly altered the chemical composition of different parts of the region surrounding the driving outflow. The CS and NH_3 abundances in the immediate vicinity of IRAS 05451+0037 have apparently significantly increased, as has the abundance of HCO^+ in the region where the redshifted lobe of the outflow has impacted the surrounding quiescent gas. It is less clear whether the abundance of $C^{18}O$ has actually been decreased in any clumps, although this is suggested weakly by the absence of a local maximum in the vicinity of the infrared source.

5. CONCLUSIONS

We have observed the central portion of the NGC 2071(N) region in millimeter lines of CO, ^{13}CO, $C^{18}O$, CS, and HCO^+, and have used existing observations of NH_3 to obtain the distribution of these different species and information on the structure of this region. We have found the morphologies of the various tracers to be quite different. As a result of the variations in fractional abundance that we feel are indicated by the observations, the quantitative conclusions about the mass and H_2 column density of different regions that we obtain are limited. We can summarize our results as follows:

1. The ^{12}CO emission at the ambient cloud velocity is relatively uniform and extended, implying gas temperatures of 11–14 K. ^{12}CO red- and blueshifted emission is detected, exhibiting a somewhat ill-defined bipolar form centered on the *IRAS* source 05451+0037. The morphology is suggestive of the hollow cone geometry discussed by Cabrit & Bertout (1986).

2. The ^{13}CO emission is less uniform than the ^{12}CO emission, with several local maxima having intensity 20%–40% above the average of the region. The relatively large intensity of the ^{13}CO, one-half that of the ^{12}CO, suggests that it is optically moderately thick, having $\tau \approx 0.7$. This explains the relatively low contrast of the ^{13}CO emission compared with that seen in the C^{18}O emission.

3. The C^{18}O integrated emission has relatively high contrast, consistent with its being optically thin, and shows four well-defined local maxima. Assuming that the fractional abundance of C^{18}O relative to H_2 is equal to 1.7×10^{-7}, we find that these clumps have masses of approximately 5 $M_\odot$, and are unbound. There is no significant C^{18}O maximum at the position of the *IRAS* source.

4. The CS emission, in contrast, is relatively concentrated in a single region having a maximum very close to the *IRAS* source. If we assume that the C^{18}O abundance there is the same as in the remainder of the cloud, the CS fractional abundance must be increased to $(2\text{–}4) \times 10^{-8}$, approaching an order of magnitude greater than the abundance typically found in molecular clouds.

5. The NH_3 emission is also highly nonuniform. Four well-isolated clumps are seen in a relatively small region, only one of which coincides with a local maximum in the C^{18}O emission. The strongest peak occurs at the location of the *IRAS* source; we suggest that it is again an increase in fractional abundance that is primarily responsible for the observed morphology of the emission from this species.

6. The HCO$^+$ emission shows up essentially as a single clump located near the maximum of the redshifted ^{12}CO emission. This location does not coincide with enhancements of any of the other species studied, and is most likely an effect of the wind on the chemical composition of the ambient cloud material. This association is supported by the HCO$^+$ line-center velocity being significantly redshifted relative to that of the equiescent cloud.

Given the great dissimilarity of the appearance of the different tracers that we have studied, and the apparent inability of excitation or radiative transfer effects to reproduce the present observations, we conclude that a significant variation in the fractional abundance of the different tracers other than C^{18}O is the most plausible explanation. While we are unable to determine the fractional abundance of the different species accurately because of the lack of information about the local density, we feel that there has been an order-of-magnitude increase in the fractional abundance of CS and NH_3 in the vicinity of the *IRAS* source. The highly fragmented appearance of the C^{18}O and NH_3 emission in the region of the outflow, and the fact that at least the C^{18}O clumps are unbound, suggest that we are witnessing the effect of nonequilibrium chemistry in an evolving region, and that a considerable fraction of the observed structure is a result of the inhomogeneous chemical composition of the region at one particular time. This is a characteristic that in a general sense is consistent with studies of other molecular clouds with ongoing star formation. It indicates that understanding the chemistry in these regions may well be a necessary prerequisite for unraveling their physical structure and evolution.

We thank S. Charnley for his comments on chemical processes relevant to the observations presented here, and W. Langer and Taoling Xie for a number of very helpful suggestions. We also thank the referee for several constructive points. The Five College Radio Astronomy Observatory is operated with the permission of the Metropolitan District Commission, and with the support of the National Science Foundation under grant AST-88-15406. This is Contribution No. 765 of the Five College Astronomy Department.

REFERENCES

Anthony-Twarog, B. J. 1982, AJ, 87, 1213

Bachiller, R., Menten, K. M., & del Rio-Alvarez, S. 1990, A&A, 236, 461

Benson, P. J., & Myers, P. C. 1983, ApJ, 270, 589

Cabrit, S., & Bertout, C. 1986, ApJ, 307, 313

Cabrit, S., Goldsmith, P. F., & Snell, R. L. 1988, ApJ, 334, 196

Charnley, S. B., Dyson, J. E., Hartquist, T. W., & Williams, D. A. 1990, MNRAS, 243, 405

Charnley, S. B., & Williams, D. A. 1990, in Molecular Astrophysics: A Volume Honouring Alexander Dalgarno, ed. T. Hartquist (Cambridge: Cambridge Univ), chap. 17

Dalgarno, A. 1985, in Molecular Astrophysics, ed. G. H. F. Diercksen, W. F. Huebner, & P. W. Langhoff (Dordrecht: Reidel), 281

Danby, G., Flower, D. R., Valiron, P., Schilke, P., & Walmsley, C. M. 1988, MNRAS, 235, 229

Draine, B. T., Roberge, W. G., & Dalgarno, A. 1983, ApJ, 264, 485

Frerking, M. A., Langer, W. D., & Wilson, R. W. 1982, ApJ, 262, 590

Fukui, Y., Sugitani, K., Takaba, H., Iwata, T., Mizuno, A., Ogawa, H., & Kawabata, K. 1986, ApJ, 311, L85

Goldsmith, P. F. 1991, in IAU Symp. 147, Fragmentation of Molecular Clouds and Star Formation, ed. E. Falgarone, F. Boulanger, & G. Duvert (Dordrecht: Kluwer), 177

Goldsmith, P. F., & Langer, W. D. 1978, ApJ, 222, 881

Goldsmith, P. F., Langer, W. D., & Wilson, R. W. 1986, ApJ, 303, L11

Goldsmith, P. F., Snell, R. L., Hasegawa, T., & Ukita, N. 1987, ApJ, 314, 525

Green, S., & Chapman, S. 1978, ApJS, 37, 169

Guélin, M. 1988, in Molecules in Physics, Chemistry, and Biology, Vol. 2, ed. J. Maruani (Dordrecht: Kluwer), 175

Herbig, G. H., & Kuhi, L. V. 1963, ApJ, 137, 398

Hildebrand, R. H. 1983, QJRAS, 24, 267

Irvine, W. M., Goldsmith, P. F., & Hjalmarson, Å. 1987, in Interstellar Processes, ed. D. Hollenbach & H. Thronson (Dordrecht: Reidel), 562

Iwata, T., Fukui, Y., & Ogawa, H. 1988, ApJ, 325, 372 (IFO)

Kutner, M. L., & Ulich, B. L. 1981, ApJ, 250, 341

Linke, R. A., Goldsmith, P. F., Wannier, P. G., Wilson, R. W., & Penzias, A. A. 1977, ApJ, 214, 50

Lis, D. C., & Goldsmith, P. F. 1991, ApJ, 369, 157

MacLaren, I., Richardson, K. M., & Wolfendale, A. W. 1988, ApJ, 333, 821

Mitchell, G. F. 1984, ApJS, 54, 81

Mitchell, G. F., & Deveau, T. J. 1982, in Regions of Recent Star Formation, ed. R. Roger & P. Dewdney (Dordrecht: Reidel), 117

———. 1983, ApJ, 266, 646

Monteiro, T. S. 1985, MNRAS, 214, 419

Nejad, L. A. M., Williams, D. A., & Charnley, S. B. 1990, MNRAS, 246, 183

Penzias, A. A. 1975, in Les Houches Session 26, Atomic and Molecular Physics and the Interstellar Matter, Course 7, ed. P. Balian et al. (Amsterdam: North-Holland), 403

Plambeck, R., & Wright, M. C. H. 1988, in Molecular Clouds in the Milky Way and External Galaxies, ed. R. Dickman, R. Snell, & J. Young (Berlin: Springer), 182

Rudolph, A., & Welch, W. J. 1988, ApJ, 326, L31

Scoville, N. Z., & Kwan, J. 1976, ApJ, 206, 718
Snell, R. L. 1989, in Structure and Dynamics of the Interstellar Medium, ed. G. Tenorio-Tagle, M. Moles, & J. Melnick (Berlin: Springer), 231
Swade, D. A. 1989a, ApJ, 345, 828
———. 1989b, ApJS, 71, 219
Tenorio-Tagle, G. 1982, in Regions of Recent Star Formation, ed. R. S. Roger & P.E. Dewdney (Dordrecht: Reidel), 1
Vogel, S. N., Genzel, R., & Palmer, P. 1987, ApJ, 315, 355
Wouterloot, J. G. A., Walmsley, C. M., & Henkel, C. 1988, A&A, 203, 367
Zhou, S., Evans, N. J., II, Güsten, R., Mundy, L. G., & Kutner, M. L. 1991, ApJ, 372, 518
Zhou, S., Evans, N. J., II, & Mundy, L. G. 1990, ApJ, 355, 159
Zhou, S., Wu, Y., Evans, N. J. II, Fuller, G. A., & Myers, P. C. 1989, ApJ, 346, 168